Supporting information for:

"Organic aerosol formation from 222 nm germicidal light: ozone-initiated vs. non-ozone pathways"

Matthew B. Goss[1,2,3] and Jesse H. Kroll[1,4]

[1]Department of Civil and Environmental Engineering, Massachusetts Institute of Technology, Cambridge, Massachusetts 02139, United States
[2]Now at Harvard University Center for the Environment, Harvard University, Cambridge, Massachusetts 02138, United States
[3]Now at John A. Paulson School of Engineering and Applied Sciences, Harvard University, Cambridge, Massachusetts 02138, United States
[4]Department of Chemical Engineering, Massachusetts Institute of Technology, Cambridge, Massachusetts 02139, United States

S.1. Estimation of 222 nm light fluence rate

For mini chamber experiments, GUV_{222} fluence rate is estimated to be 45 μW cm^{-2} based on Barber et al.[1] which used the same experimental setup. This was based data from the manufacturer and a simple geometric representation of the chamber, and is supported by strong agreement between a simple model and the measured ozone production. The ozone production rate in the mini chamber was quantified as 324 ppb hr^{-1} by fitting the data to equation S1.

$$[O_3](t) = \frac{P_{O_3}}{k}(1 - e^{-kt}) \#(S1)$$

For large chamber experiments, GUV_{222} fluence rate is estimated by comparing measured ozone production rate from a blank experiment ("big_222_blank_dry" (expt. 1)) to that measured previously in the mini chamber. Fitting this curve yields a measured ozone production rate of 27.9 ppb hr^{-1}. Based on the GUV_{222} fluence rate of the mini chamber, this implies an average GUV_{222} fluence rate of 3.9 μW cm^{-2}.

Table S1: Summary of basic experimental setups. Columns identify the light/oxidant conditions, the dilution air source, and whether the CAPS NO_2, NO_X analyzer, and NH_4^+ CIMS were used.

Exp. number	Date	Experiment name	Light/oxidant	Chamber	Dilution air source[a]	CAPS NO_2	NO_X analyzer	NH_4^+ CIMS
1	2023-08-22	big_222_blank_dry	222 nm	big	AADCO	-	Y	-
2	2023-08-23	big_O3_blank_dry	O_3	big	AADCO	-	Y	-
3	2023-08-24	big_222_lim_dry	222 nm	big	AADCO	-	Y	-
4	2023-08-25	big_O3_lim_dry	O_3	big	AADCO	Y	Y	-
5	2023-08-26	big_222_lim	222 nm	big	AADCO	Y	Y	-
6	2023-08-27	big_O3_lim	O_3	big	AADCO	Y	Y	-
7	2023-08-28	big_222_lim_HONO	222 nm	big	AADCO	Y	Y	-
8	2023-09-03	mini_222_lim_1	222 nm	mini	AADCO	-	Y	-
9	2023-09-03	mini_O3_lim_1	O_3	mini	AADCO	-	Y	-
10	2023-09-03	mini_222_lim_2	222 nm	mini	AADCO	-	Y	-
11	2023-09-03	mini_O3_lim_2	O_3	mini	AADCO	-	Y	-
12	2023-09-05	mini_222_lim_3	222 nm	mini	AADCO	Y	Y	-
13	2023-09-05	mini_O3_lim_3	O_3	mini	AADCO	Y	Y	-
14	2023-09-05	mini_blank_aadco_old	222 nm	mini	AADCO	Y	Y	-
15	2024-01-31	mini_222_lim_dry_1	222 nm	mini	UZA	-	-	-
16	2024-01-31	mini_O3_lim_dry_1	O_3	mini	UZA	-	-	-
17	2024-02-01	mini_O3_lim_dry_2	O_3	mini	UZA	-	-	-
18	2024-02-01	mini_222_lim_dry_2	222 nm	mini	UZA	-	-	-
19	2024-02-02	mini_222_lim_dry_3	222 nm	mini	UZA	-	-	-
20	2024-02-02	mini_O3_lim_dry_3	O_3	mini	UZA	-	-	-
21	2024-02-05	mini_222_lim_4	222 nm	mini	UZA	-	-	Y
22	2024-02-06	mini_O3_lim_4	O_3	mini	UZA	-	-	Y
23	2024-02-06	mini_222_lim_5	222 nm	mini	UZA	-	-	Y
24	2024-02-07	mini_O3_lim_5	O_3	mini	UZA	-	-	Y
25	2024-02-07	mini_222_lim_6	222 nm	mini	UZA	-	-	Y
26	2024-02-07	mini_O3_lim_6	O_3	mini	UZA	-	-	Y
27	2024-02-12	mini_222_lim_nox_1	222 nm	mini	UZA	Y	Y	Y
28	2024-02-12	mini_O3_lim_nox_1	O_3	mini	UZA	Y	Y	Y
29	2024-02-12	mini_222_lim_nox_2	222 nm	mini	UZA	Y	Y	Y
30	2024-02-12	mini_O3_lim_nox_2	O_3	mini	UZA	Y	Y	Y
31	2024-02-12	mini_222_lim_nox_3	222 nm	mini	UZA	Y	Y	Y
32	2024-02-12	mini_O3_lim_nox_3	O_3	mini	UZA	Y	Y	Y
33	2024-02-23	mini_blank_aadco_new	222 nm	mini	AADCO	Y	Y	-
34	2024-02-23	mini_blank_UZA	222 nm	mini	UZA	Y	Y	-
35	2024-02-23	mini_222_outdoor_1	222 nm	mini	Outdoor	Y	Y	-
36	2024-02-26	mini_O3_outdoor_1	O_3	mini	Outdoor	Y	Y	-
37	2024-02-26	mini_222_outdoor_2	222 nm	mini	Outdoor	Y	Y	-
38	2024-02-27	mini_O3_outdoor_2	O_3	mini	Outdoor	Y	Y	-
39	2024-02-27	mini_222_outdoor_3	222 nm	mini	Outdoor	Y	Y	-
40	2024-02-27	mini_O3_outdoor_3	O_3	mini	Outdoor	Y	Y	-

[a] AADCO refers to air from the clean air generator, UZA refers to ultrazero air supplied by Linde, Outdoor refers to air pumped into the chamber from outside the building as described in the main text.

Table S2: Summary of measured experimental conditions and tabulation of maximum nucleated particle concentration.

Exp. number	Experiment name	Mean RH (%)[a]	Mean T (°C)[b]	Starting limonene (ppb)[c]	Starting O_3 (ppb)[d]	Mean NO_X (ppb)[e]	Starting particle conc. (#/cm^3)	Max. nucleated particle conc. (# / cm^3)[f]
1	big_222_blank_dry	0	20	0	1.2	1.9	39000	-
2	big_O3_blank_dry	0	20	0	2.4	1.5	39000	-
3	big_222_lim_dry	0	20	81.9	4.8	1.3	22000	-
4	big_O3_lim_dry	0	20.4	89.6	1.3	1.0	22000	-
5	big_222_lim	34.7	20.1	96	1.8	1.1	21000	-
6	big_O3_lim	34.3	20.1	97.9	0.9	1.1	20000	-
7	big_222_lim_HONO	35.6	20.1	97.5	1.1	16.1	19000	-
8	mini_222_lim_1	28.7	23.5	46.1	98.9	1.9	58000	160000
9	mini_O3_lim_1	28.3	23.4	42.8	112.8	1.1	63000	0
10	mini_222_lim_2	27.8	23.7	47	111.3	1.5	70000	71000
11	mini_O3_lim_2	27.9	23.5	41.3	104.5	1.2	65000	6900
12	mini_222_lim_3	28.3	23.7	38.9	93.8	1.9	71000	38000
13	mini_O3_lim_3	28.1	23.6	21.7	96.6	1.5	57000	0
14	mini_blank_aadco_old	28.9	23.6	0	0.2	1.8	0.92	-
15	mini_222_lim_dry_1	0	-	17.7	107.3	-	20000	150000
16	mini_O3_lim_dry_1	0	-	20.1	103.7	-	20000	73000
17	mini_O3_lim_dry_2	0	-	22.3	112.4	-	21000	46000
18	mini_222_lim_dry_2	0	-	24.3	105.3	-	23000	160000
19	mini_222_lim_dry_3	0	-	24.4	101.8	-	17000	200000
20	mini_O3_lim_dry_3	0	-	20.4	107.2	-	17000	93000
21	mini_222_lim_4	35.6	-	39.3	102	-	27000	57000
22	mini_O3_lim_4	35.6	-	40.4	114.5	-	27000	2800
23	mini_222_lim_5	35.6	-	41.7	110.6	-	27000	43000
24	mini_O3_lim_5	35.6	-	41.9	111.8	-	19000	8500
25	mini_222_lim_6	35.7	-	41.7	105.1	-	21000	53000
26	mini_O3_lim_6	33.7	-	37.4	108.6	-	23000	14000
27	mini_222_lim_nox_1	33.1	-	41.8	79.4	17.3	23000	10000
28	mini_O3_lim_nox_1	33.1	-	31.1	79.9	17.9	23000	0
29	mini_222_lim_nox_2	33.2	-	41.1	89.6	18.1	25000	4400
30	mini_O3_lim_nox_2	33.2	-	40.8	79.6	18.4	24000	0
31	mini_222_lim_nox_3	33.5	-	42.2	87.9	18.7	26000	2300
32	mini_O3_lim_nox_3	33.5	-	43.1	82.8	19.0	27000	0
33	mini_blank_aadco_new	28	-	0	-1.0	0.7	0	-
34	mini_blank_UZA	27.1	-	0	1.0	0.6	0.52	-
35	mini_222_outdoor_1	45.3	-	0	2.4	17.5	6.8	-
36	mini_O3_outdoor_1	41.2	-	0	7.0	6.1	11	-
37	mini_222_outdoor_2	42.2	-	0	6.8	8.2	11	-
38	mini_O3_outdoor_2	43.7	-	0	0.4	15.2	14	-
39	mini_222_outdoor_3	45.2	-	0	1.3	18.6	32	-
40	mini_O3_outdoor_3	45	-	0	0.6	22.4	64	-

[a] For dry experiments, measured relative humidity was slightly below 0. This is reported as 0 here.

[b] Temperature was accidentally not logged for most mini chamber experiments. In all cases, the chamber temperature was the same as room temperature (~24 °C).

[c] Starting limonene is based on the GC signal and reported as the linearly interpolated concentration at t = 0 (big chamber), or the concentration derived from the first GC point after the start of the experiment (mini chamber) (see Fig. S3).

[d] Starting ozone is the average ozone concentration for 500 seconds before t = 0.

[e] Mean NO_X is the average total NO_X as measured by the Thermo Scientific NO_X monitor (note that this includes HONO), averaged from t = 0 to t = 5 hrs (big chamber) or t = 55 min (mini chamber). NO_X was not measured for some experiments where no NO_X was added.

[f] Max. nucleated particle concentration is shown in Figure 1 in the main text and discussed in Section S.4. This value is only applicable to mini chamber limonene experiments.

S.2. Additional experimental methods

Chamber dilution rate is monitored by measuring the loss of hexafluorobenzene using the GC-FID. For small chamber experiments, this is measured to be 7.6 ± 0.1 × 10^{-4} s^{-1} (2023 experiments) or 9.0 ± 0.2 × 10^{-4} s^{-1} (2024 experiments) (all listed uncertainties in the supporting information are 1σ). While all experiments use the same flow rate set by a mass flow controller, a leak in the bubbler used for the 2023 experiments caused the real dilution rate to be slightly lower. For outdoor air experiments, the same flow rate setpoints as the standard humid chamber experiments are used, such that the flow of outdoor air is split directly into the chamber (6.9 LPM) and through a bubbler (3.6 LPM) resulting in a relative humidity of 41-45%. For large chamber experiments, the measured dilution rate is 4.42 ± 0.09 × 10^{-5} s^{-1}.

To minimize variability between mini chamber experiments, steady-state ozone is matched between GUV_{222} and ozone-only experiments. For NO_X-free experiments starting ozone is 104 ± 6 ppb for GUV_{222} and 108 ± 6 ppb for the ozone-only conditions. While these exhibit some variability, the difference in starting ozone under the two different conditions is not statistically significant (p = 0.15).

To further minimize variability, additions to the mini chamber are carefully timed. A solution of ammonium sulfate (>99% purity, Sigma Aldrich) in Milli-Q water (2 g/L) is atomized for exactly 45 seconds for all mini chamber experiments, but measured seed concentration is much higher for 2023 experiments (6.4 ± 0.6 × 10^4 particles cm^{-3} for 2023 experiments, 2.3 ± 0.3 × 10^4 particles cm^{-3} for 2024 experiments). This is likely due at least in part to higher particle wall loss rates in 2024 caused by static electricity build-up during maintenance. Approximately 2-4 minutes after the seed aerosol addition, hexafluorobenzene (0.05 µL, 70 ppb, 99% purity, Thermo Scientific) is added. Approximately 3-5 minutes later, (*R*)-(+)-limonene (0.1 µL, 100 ppb, 97% purity, Sigma Aldrich) is added, initiating the experiment. Timing on later experiments (after "mini_222_lim_4" (expt. 21)) is more tightly controlled such that addition times vary by less than 5 seconds.

For the mini chamber experiments with added NO_X, NO is introduced to the chamber via a steady 120 sccm flow from a 1.93 ppm tank (Linde). This rapidly converts to NO_2 through reaction with ozone, resulting in a steady-state NO_X concentration of 18.2 ± 0.7 ppb. The steady state ozone concentration is suppressed to 86 ± 6 and 81 ± 2 ppb for GUV_{222} and ozone-only experiments respectively.

For experiment 7, nitrous acid (HONO) is prepared via reaction of sodium nitrite and sulfuric acid. Sodium nitrite (1.74 g, >99% purity, Sigma Aldrich) is dissolved into 25 mL of Milli-Q water in a three-necked round bottom flask with a stir bar. Sulfuric acid (1 M, 50 µL) is drawn up into a syringe and placed into a syringe pump with a tube feeding directly into the sodium nitrite solution. Clean air is flowed over the stirred liquid at 1 LPM, and sulfuric acid is added in two additions of 3.9 µL at 2 µL/min. This is sufficient to reach [HONO] ≈ 10 ppb in the large chamber after about 45 minutes, with minimal NO and NO_2 which can sometimes be byproducts of this reaction. For this experiment, the 222 nm light was then turned on, and sulfuric acid flow was set to a continuous 0.023 µL/min to maintain an approximate steady-state HONO concentration. See Fig. S8 for a graphical representation of the HONO timeseries.

S.3. Instrument details and detailed description of data analysis methods

Particle size and concentration measurements are carried out using a scanning mobility particle sizer (SMPS, TSI). The SMPS consists of a differential mobility analyzer (DMA, Model 3082), paired with a condensation particle counter (CPC, Model 3775). Sheath flow is set to 3 LPM while sample flow is set to 0.3 LPM, enabling detection of particles with a size range of 15 – 685 nm. SMPS data is processed with the Aerosol Instrument Manager 10.3.1.0 software from TSI.

Particle composition measurements are taken using an aerosol mass spectrometer (AMS, Aerodyne Research, Inc.). Ionization efficiency and relative ionization efficiency calibrations were carried out before the two series of experiments in 2023 and 2024. AMS data were processed using SQUIRREL 1.63B and PIKA 1.23B. Elemental analysis of high-resolution AMS data was carried out using the improved ambient elemental analysis method from Canagaratna et al.[2] For large chamber experiments, AMS HR aerosol species timeseries were exported and corrected for wall loss and dilution loss by normalizing to the loss of the ammonium sulfate seed particles (see Wang et al.[3] eq. 4). The corrected timeseries are then scaled such that initial aerosol seed concentration matches that measured by the SMPS. AMS mini chamber experiments are not corrected for wall- and dilution-loss since high particle loss rates make such corrections highly uncertain.

A gas chromatograph with flame ionization detection (GC-FID, SRI Instruments) was used to measure limonene and hexafluorobenzene, the dilution tracer. The GC-FID method is nearly the same as that published in Goss and Kroll,[4] except that the method is lengthened by one minute to ensure that limonene is detected. For the first limonene experiment (exp. 3), an oven cooling time of 4.75 minutes was used; to reduce the total duty cycle, cooling time was reduced to 1 minute for the second limonene experiment (exp. 4) but this resulted in inconsistent limonene retention times. All subsequent experiments used a cooling period of 2 minutes, resulting in a total duty cycle of 12 minutes.

GC-FID data was processed in R to ensure consistent integration across samples. The chromatograph baseline was calculated using the R package “baseline” and the asymmetric least squares method (lambda = 6, p = 0.0001).[5] Hexafluorobenzene (HFB) elutes around 6.2 to 6.3 minutes as a single distinct peak. Despite the use of a new bottle of limonene (97% purity, Sigma Aldrich), limonene is detected as several peaks from about 8.3 to 9.5 minutes. We believe this is likely due to reaction of limonene inside the GC trap or potassium iodide ozone scrubber in the sample line. The distribution of peaks changes slightly with relative humidity, and changes slightly as each experiment proceeds, but is otherwise largely the same, even between experiments carried out several months apart. While this introduces some additional uncertainty into limonene quantification, no differences in the peak distribution are seen between matching GUV_{222} and ozone control conditions. For all experiments, the areas of these peaks are summed to give an effective limonene peak area.

GC-FID limonene and HFB sensitivity are calculated based on a series of known volume injections into the large chamber. In addition to injections in the five large-chamber limonene oxidation experiments, three additional injections were carried out when the chamber was dry, and three injections were carried out when the chamber was humid (~35% RH). No difference in sensitivity was observed between dry and humid conditions. After one outlier was removed, limonene sensitivity was found to be 46.2 ± 1.7 mV s ppb^{-1}. HFB sensitivity was 30.8 ± 0.9 mV s ppb^{-1}. Based on the consistency of limonene and HFB

peak areas between 2023 and 2024 mini-chamber experiments, these do not seem to have drifted substantially over time. Limonene and HFB concentrations are estimated by dividing measured GC area by the sensitivity.

The total volumes of limonene added to chambers (large: 6.0 µL, mini: 0.1 µL) correspond to 119 ppb and 100 ppb respectively, but measured concentrations appear lower in the mini chamber, likely due to non-instantaneous evaporation of limonene (see Figures S3 and S9). For large chamber experiments, a heated inlet was used and limonene was allowed to diffuse into the chamber before the experiment started; it could take as much as ~45 minutes for the limonene concentration to stabilize. For mini chamber experiments, the inlet was not heated and the experiment started as soon as limonene was added, such that limonene likely continued to diffuse into the chamber for the whole experiment. Despite possible increased uncertainty in the limonene concentration due to this slow diffusion, measured limonene concentration in the mini chamber is consistent within each set of experiments, with only one distinct outlier (see Figs. S3 and S9). We do however observe that measured limonene concentration is substantially lower for limonene mini chamber experiments performed under dry conditions (Fig. S3). Since the GC-FID sensitivity was not observed to be sensitive to humidity changes in the large chamber, we hypothesize that the change in humidity in the mini chamber may slightly affect limonene's rate of evaporation or adsorption to surfaces; however, the reason for this difference is unclear. The repeatability of hexafluorobenzene addition to the mini chamber (7.5% relative standard deviation for a 0.05 µL addition) suggests that the total volume of limonene added (0.1 µL) should overall be quite consistent, even if slightly affected by variable evaporation or adsorption rates.

NO, NO_2, and HONO are measured by a combination of the NO_X analyzer (Thermo Fisher Scientific) and the CAPS NO_2 monitor (Aerodyne Research, Inc.). NO is measured directly by the NO_X analyzer and NO_2 is selectively measured by the CAPS NO_2 monitor. The NO_X analyzer also converts NO_2 and HONO to NO using a molybdenum catalyst, and measures this as total "NO_X." By subtracting measured NO and NO_2 from this total "NO_X" measurement, we obtain a measurement of HONO. We assume that all of this remainder is HONO but this measurement may also be influenced by other species such as organonitrates or peroxyacetyl nitrates.

For two sets of mini chamber experiments (exp. 21 – 32), an ammonium chemical ionization mass spectrometer (NH_4^+ CIMS; modified PTR3[6]) was used to examine trends in oxidized organics. The instrument was not fully functional during these experiments, due to a low, unstable primary ion signal, and therefore no attempt is made to calibrate the data to concentration units. However, unit mass resolution data taken directly from raw files saved by the Tofwerk TofDAQ Recorder were used to provide qualitative information about the temporal behavior of high-mass gas-phase oxidized organic species. These results are plotted in Figure S18 and discussed further in section S.9.

S.4. New particle formation analysis

As described briefly in the main text, new particle formation is quantified by fitting the observed size distribution modes in the SMPS data to lognormal distributions. This analysis is carried out only for limonene mini chamber experiments, since no nucleation was observed in large chamber experiments, and no seed particles were added for outdoor air experiments. The analysis is applied to the first 15 minutes of each experiment since the greatest particle number concentrations are observed during this time.

Using the logarithm of the particle diameter as an x-axis, data are fit to both one and two normal distributions using the "normalmixEM" function from the "mixtools" package in R.[7] To improve the fit, measured points below $dN/d\log(D_p) = 5000$ are removed. The resulting fit gives the center and standard deviation of each distribution; the amplitude for each curve is optimized using a linear fit of the data against the two fitted curves. Trends in r^2 for the one- and two-mode fit can be used to identify timepoints where a nucleation mode appears. With only one mode, r^2 is high for both the one- and two-mode fit. With two modes, r^2 for the one-mode fit drops consistently below that for the two-mode fit. This is backed up visually: due to the substantial separation in particle diameter between the two modes, data where new particle formation has occurred is easily identified.

Example fitted curves are plotted in Figure S1A, demonstrating relatively good fit to the data. The curves are then integrated to obtain total particle number concentrations attributed to each mode, as shown in Figure S1B. The maximum of the particle number concentration attributed to the nucleation mode is considered to be the maximum total new particle formation for purposes of comparing nucleation between experiments (See Figure 1B in the main text, and Table S2). For experiments where a nucleation mode is not observed, this value is considered to be 0. Two mode fits to the timepoints assigned to the maximum total new particle formation have a mean $r^2 = 0.97 \pm 0.01$.

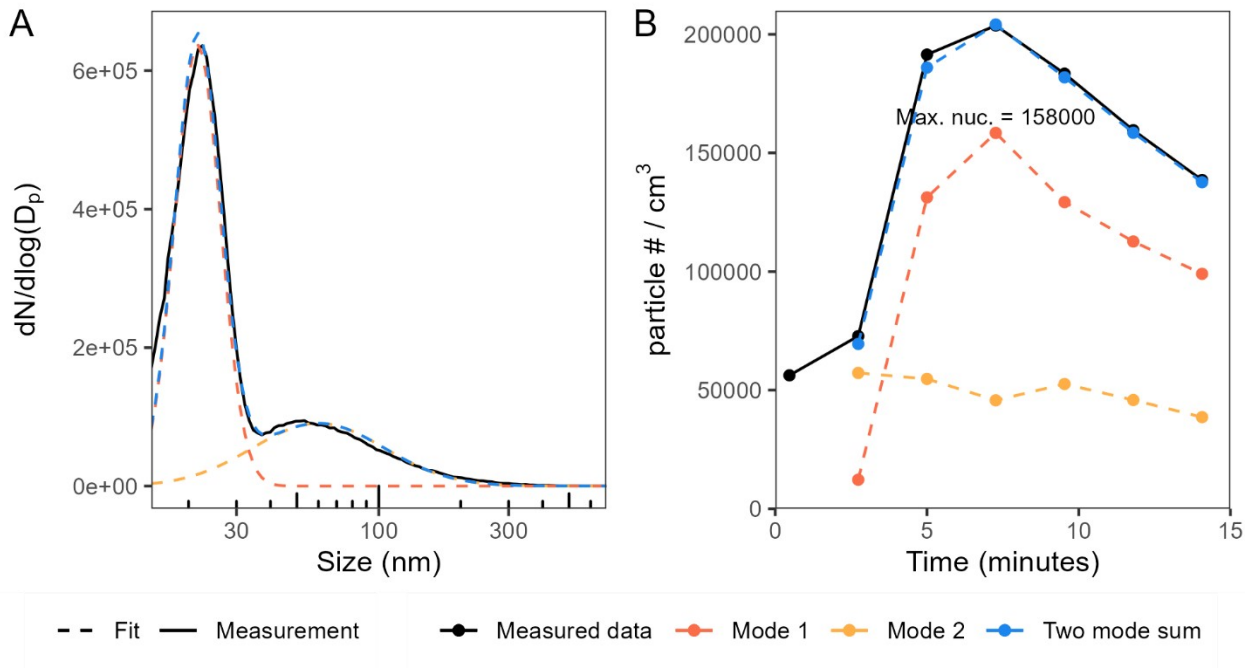

Figure S1: Example of particle size distribution mode analysis for "mini_222_lim_1" (expt. 8). Panel A shows the size distribution from the point at t = 5 minutes, overlaid with fits of the two modes, and the sum of these two fits. Panel B shows a timeseries of the measured total particle concentration, overlaid with the integrated particle number from the fits of both modes, and the sum of the particle number derived from these two fits. Fitted data is not shown for the first data point because a second mode had not yet appeared. Panel B is also labeled with the maximum nucleated particle concentration for this experiment.

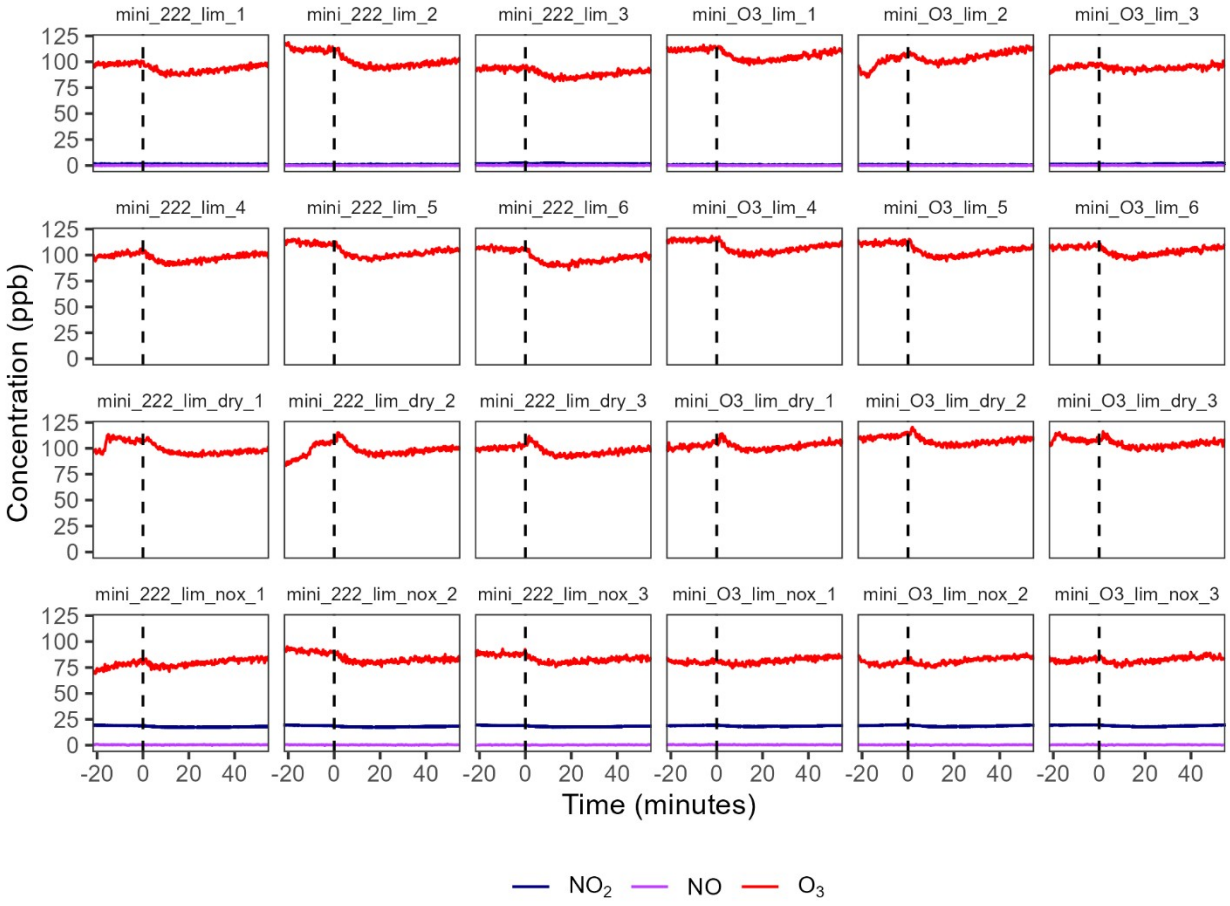

Figure S2: Ozone and NO_X measurements for each limonene mini chamber experiment. Each row corresponds to an experiment set. The left three columns correspond to GUV_{222} experiments and the right three columns correspond to ozone-only experiments. Note that NO_X is not measured for all experiments. NO_2 measurements are from the CAPS NO_2 instrument with the exception of experiments 8 – 11 where NO_2 measurements are taken from the NO_X analyzer. The dashed line marks t = 0 (the time at which limonene is added to the chamber). Inconsistencies seen in the ozone concentration before t = 0 for some experiments are from the switch between using the 222 nm as an ozone source, and using the ozone generator as an ozone source. For dry experiments, the ozone concentration appears to rise slightly around t = 0. This is believed to be due to cross-sensitivity of the ozone monitor to hexafluorobenzene; a similar effect is observed in dry large chamber experiments. In all experiments, the ozone concentration is briefly depressed after limonene is added.

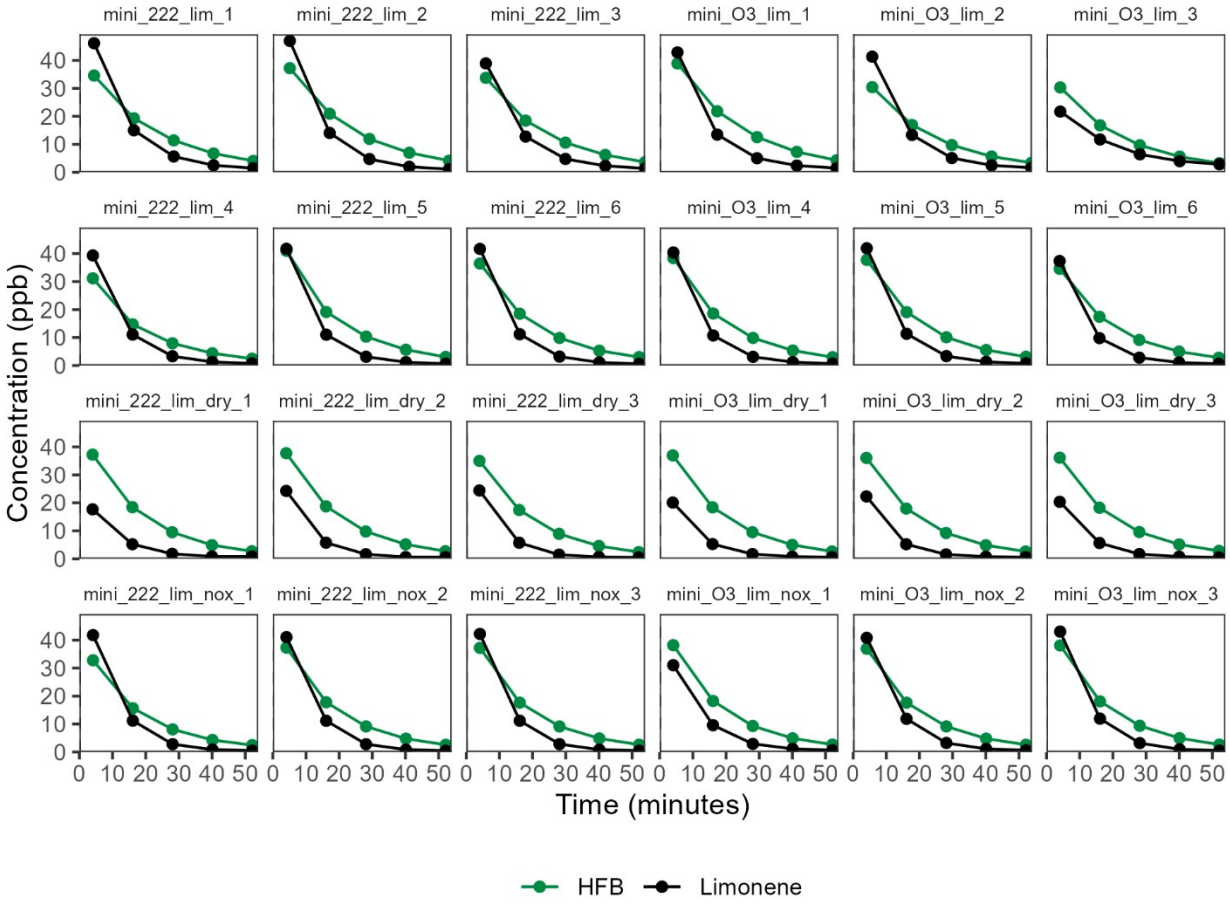

Figure S3: Limonene and hexafluorobenzene timeseries for each limonene mini chamber experiment. Concentrations are shown in ppb, based on calibrations performed in the large chamber. Calibrations and uncertainty in the limonene concentration are discussion in Section S.3. Panels are ordered in the same way as Figure S2.

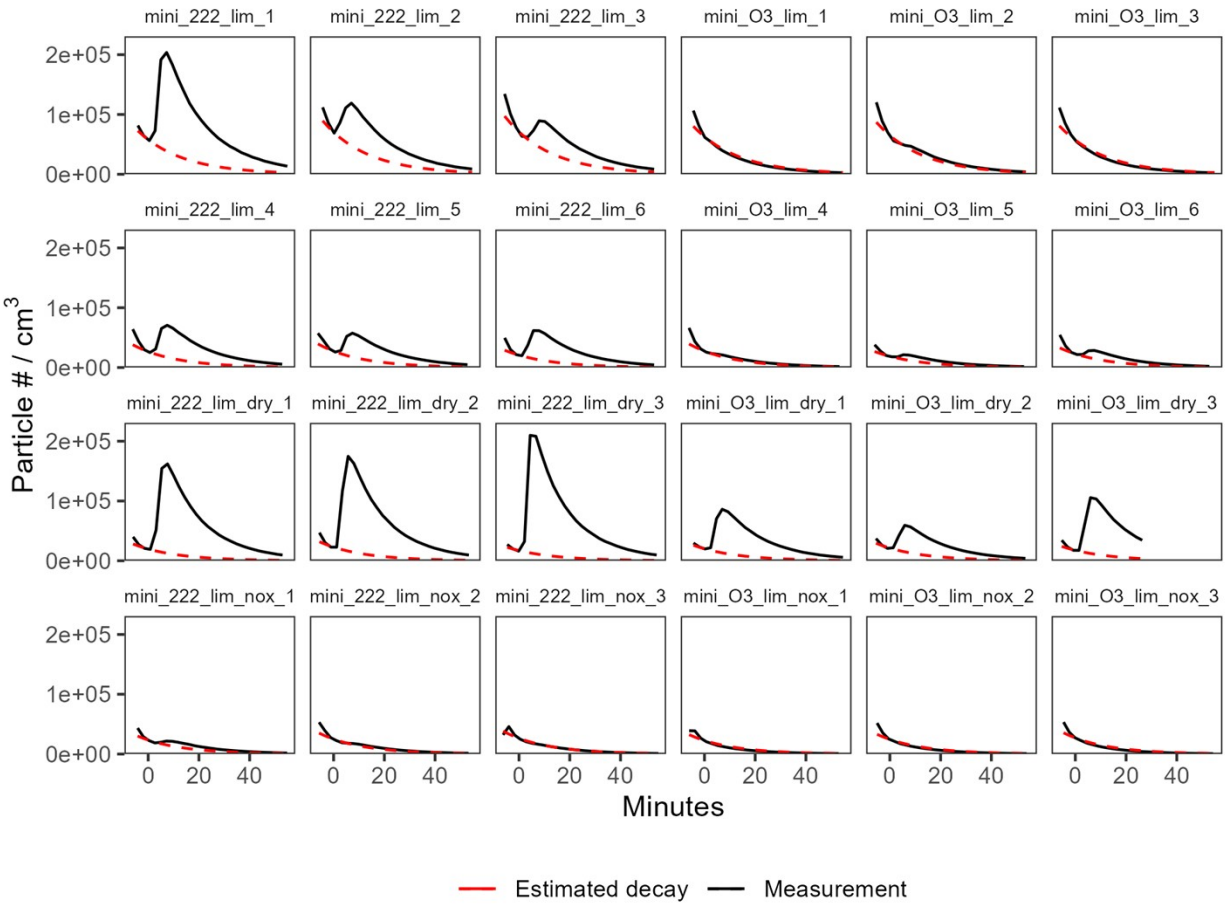

Figure S4: Total particle number concentrations for each limonene mini chamber experiment. Panels are ordered in the same way as Figure S2. Measured particle concentration is plotted in black. As an illustration of the effects of new particle formation on total particle concentration, estimated decay in the absence of new particle formation is plotted in red. These curves are an exponential function starting from the measured concentration at t = 0 with a decay rate matched to the average end-of-experiment particle loss rate (from fitting the particle loss rate after t = 1000 s; $9.3 \pm 0.2 \times 10^{-4}$ s^{-1} for 2023 experiments, $9.9 \pm 0.3 \times 10^{-4}$ s^{-1} for 2024 experiments). Where more nucleation is observed, the black line peaks well above the red line.

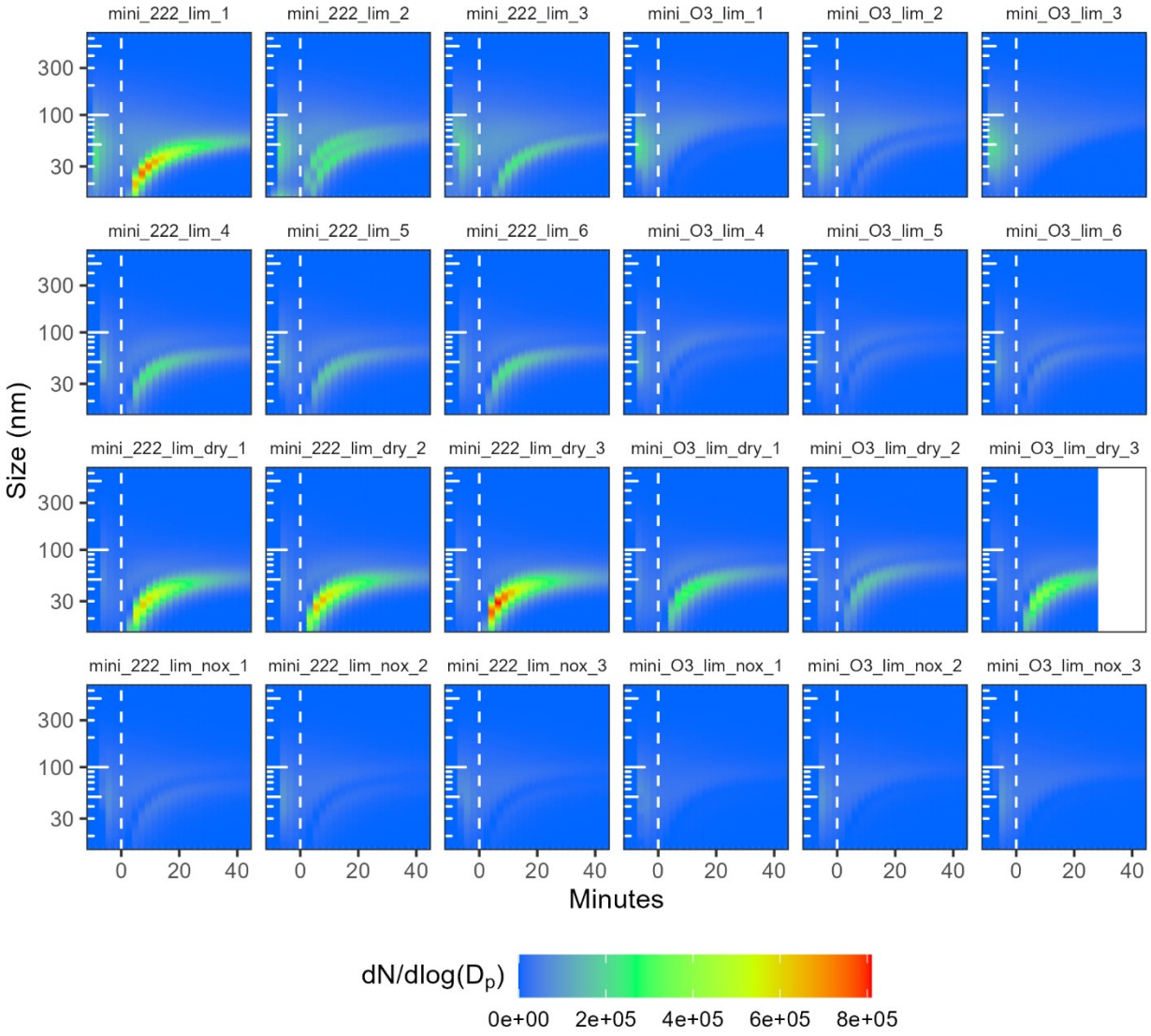

Figure S5: Number-weighted particle size concentrations for each limonene mini chamber experiment. Panels are ordered in the same way as Figure S2. The dotted white line marks t = 0 when limonene was added to the chamber. The appearance of particles several minutes before t = 0 corresponds to the addition of ammonium sulfate seed particles. Data is missing for the end of one experiment ("mini_O3_lim_dry_3" (expt. 20)) due to an instrument fault.

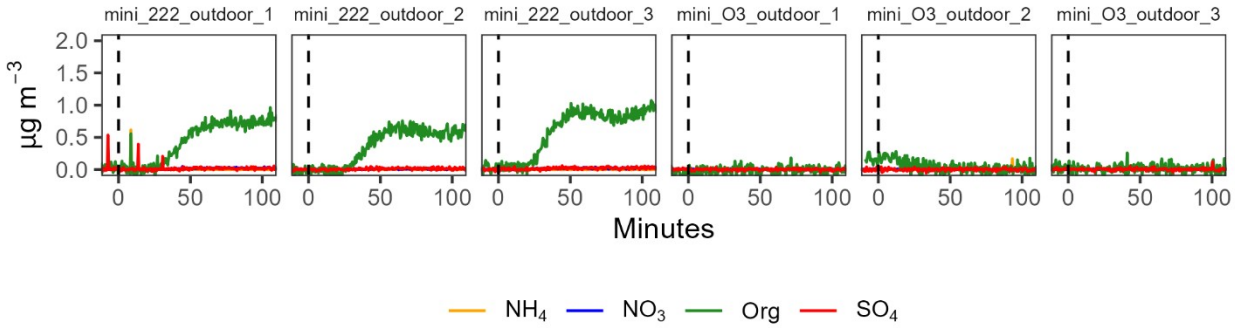

Figure S6: Aerosol composition timeseries for each outdoor air mini chamber experiment. Data are not corrected for wall loss, dilution loss, or collection efficiency. A small amount of aerosol is clearly formed during each outdoor air experiment with 222 nm light, but organic aerosol as measured by the AMS is not clearly different from zero for ozone-only conditions.

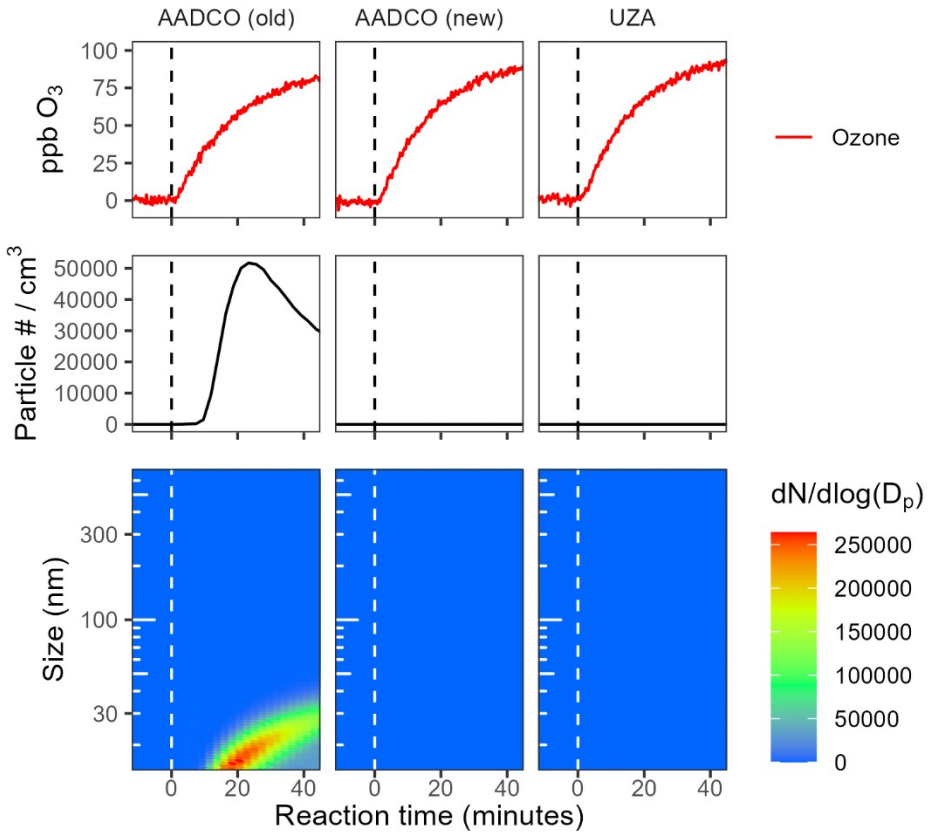

Figure S7: Particle size and ozone measurements from blank experiments with three different clean air sources. The top row shows ozone concentration, the middle row shows total particle number concentration, and the bottom row shows number-weighted particle size distribution over time. Time = 0 corresponds to the time at which the 222 nm lamp was turned on. The first column shows data from a blank experiment carried out with AADCO air before the pump replacement (expt. 14), the second column shows a blank experiment carried out with AADCO air after the pump replacement (expt. 33), and the third column shows a blank experiment where ultra zero air was used (expt. 34). As was reported in Barber et al.[1] and as is seen here, large numbers of ultrafine particles form in AADCO air before the pump replacement. With ultra zero air or a new pump, no new particle formation occurs. Ozone production appears slightly different between experiments, but may be influenced by slight variations in the chamber dilution rate.

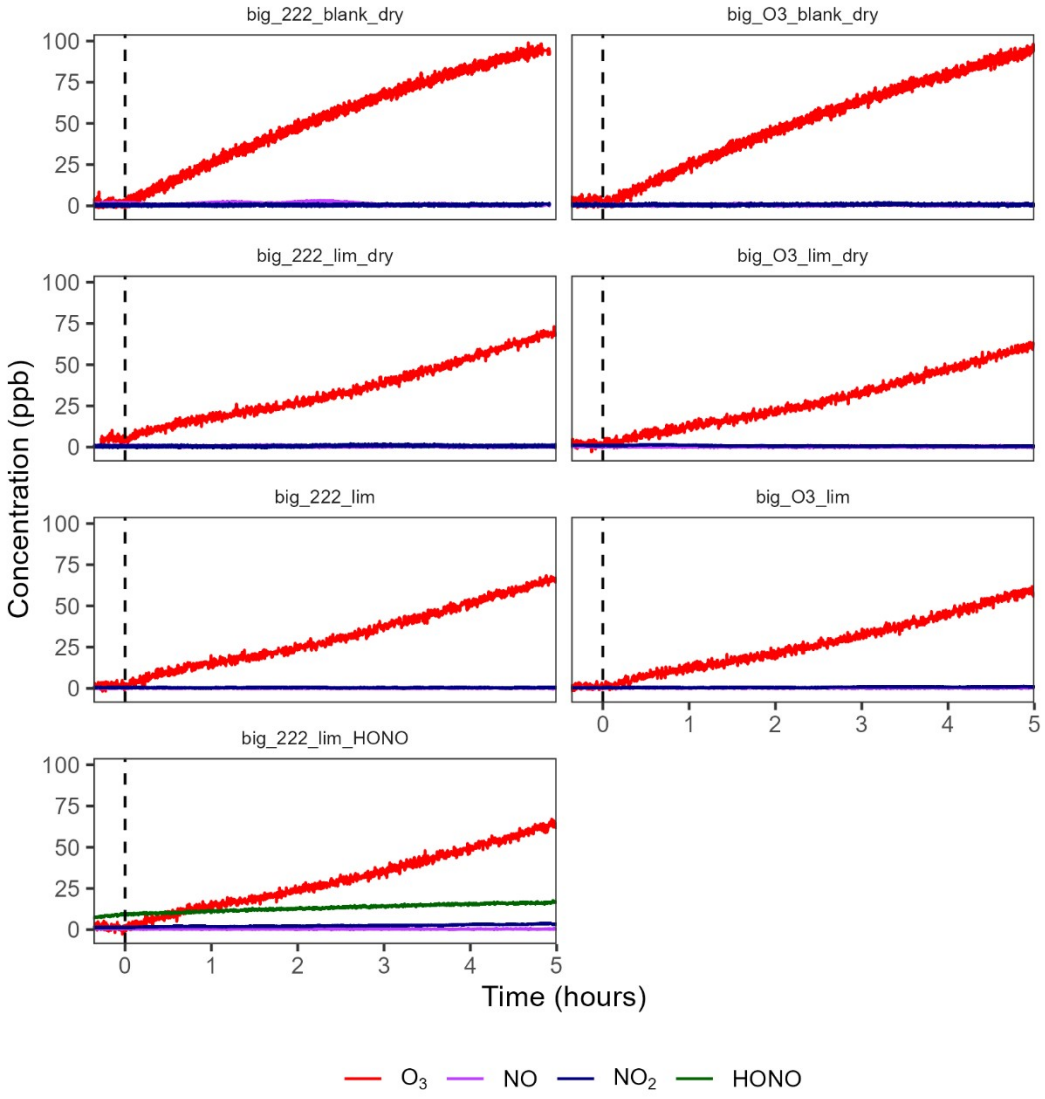

Figure S8: Ozone and NO_X measurements for each large chamber experiment. Ozone timeseries are different for the two blank experiments but match for all others, where limonene suppresses the increase in ozone. Plotted NO_2 is measured by the CAPS NO_2 monitor except for the first three experiments, in which it is measured by the Thermo Scientific NO_X monitor since the CAPS was not used. HONO is determined from the difference between the NO_X measurement and CAPS NO_2 measurement. NO_X concentrations are generally around or below the detection limit (~ 2 ppb) when NO_X is not added. The dashed line marks t = 0 (the time at which O_3 is added or 222 nm light is turned on).

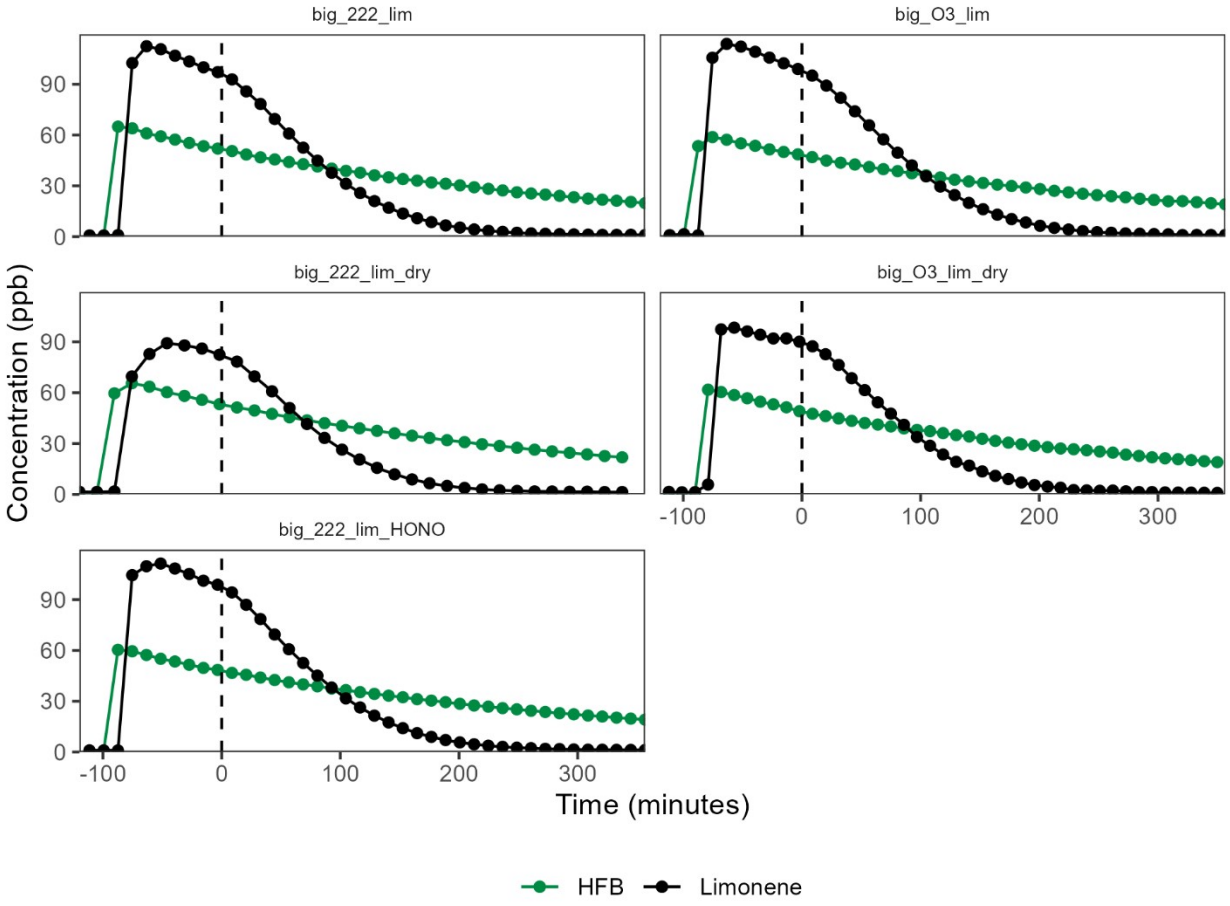

Figure S9: Limonene and hexafluorobenzene timeseries for each limonene large chamber experiment. Concentrations are shown in ppb, based on calibrations performed in the large chamber. Timeseries shown here are not dilution-corrected. Calibrations and uncertainty in the limonene concentration are discussion in Section S.3.

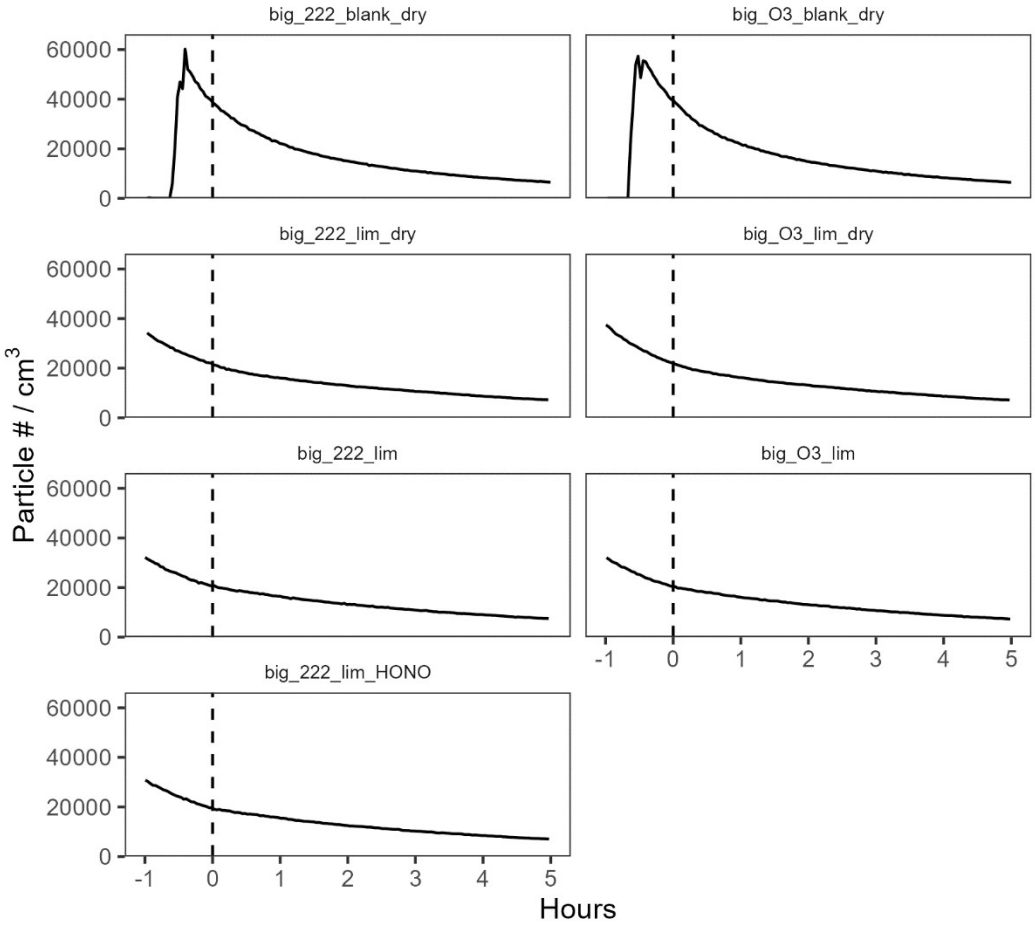

Figure S10: Total particle number concentrations for each large chamber experiment. No new particle formation is observed in these experiments.

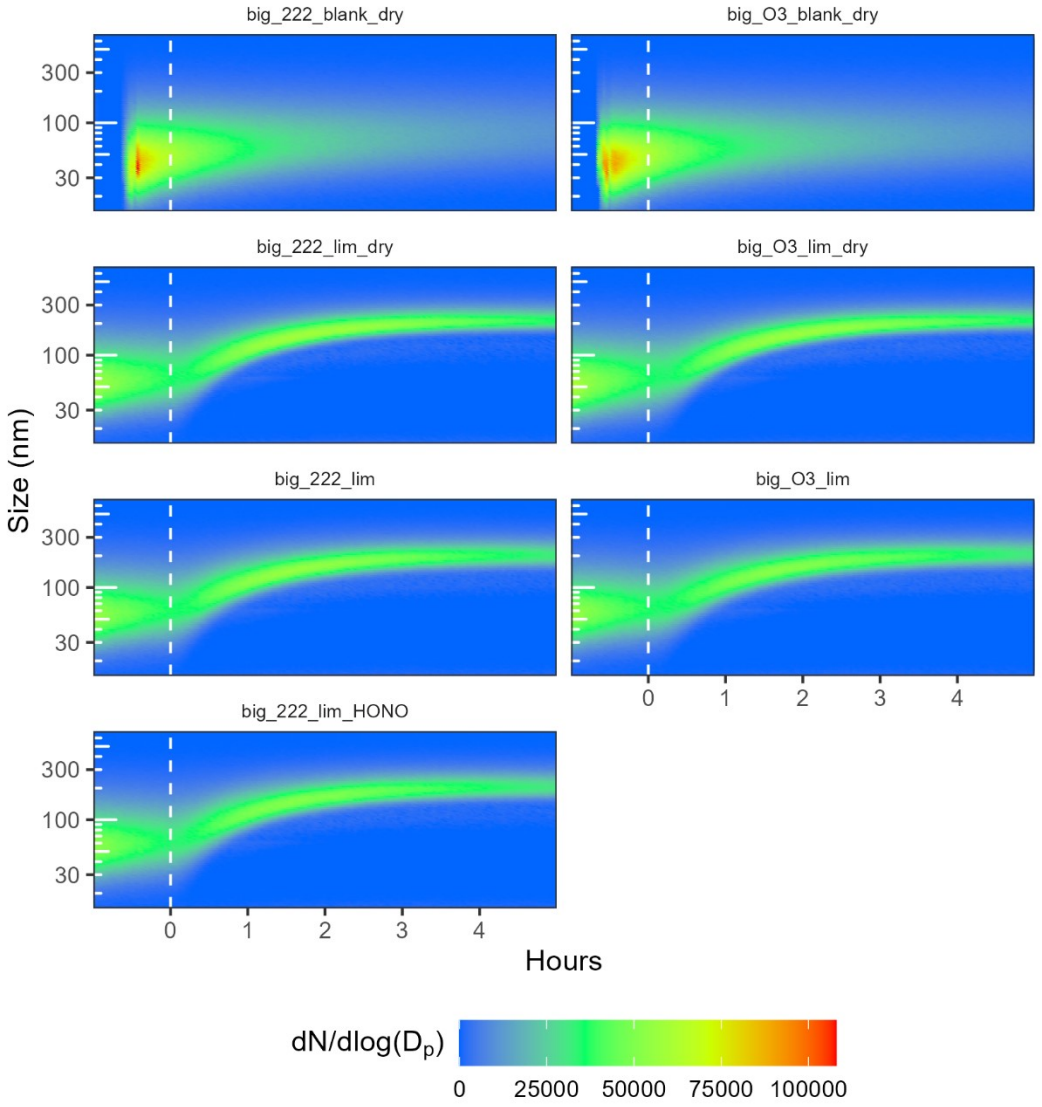

Figure S11: Number-weighted particle size concentrations for each large chamber experiment. The dotted white lines mark t = 0 when the GUV_{222} lamp or ozone generator was turned on. The appearance of particles before t = 0 corresponds to the addition of ammonium sulfate seed particles. The seed particles were added closer to t = 0 for blank experiments since monitoring VOC precursor decay before the start of the experiment was not necessary. No new particle formation is observed in these experiments and particle size distributions exhibit patterns consistent with particle growth.

Section S.5. Estimating chamber experiment condensation sinks

To compare the total condensation sink between mini and large chamber experiments, the condensation sink to particles (at the beginning of each experiment) and to chamber walls is estimated. Condensation to particles (CS) is calculated using the same approach as Krechmer et al.[8] Considering the loss of oxidized organics, the molecular weight is assumed to be 250 g mol^{-1}, the diffusion coefficient is assumed to be 6×10^{-6} m^2 s^{-1},[8] and the mass accommodation coefficient is assumed to be 1. For large chamber experiments, the estimated condensation sink to particles is 1.3 to 1.8 min^{-1}. For mini chamber experiments, this value ranges from 0.63 to 3.5 min^{-1} due to greater variation in total particle loading between sets of experiments.

Loss to chamber walls uses the same assumptions applied in the supporting information of Ye et al.[9] The large chamber has a volume of 7.5 m^3 and surface area of 23 m^3. The mini chamber has a volume of 0.15 m^3 and surface area of 2.0 m^3. The wall loss rate is estimated to be 0.09 min^{-1} and 0.4 min^{-1} for the large and mini chamber respectively.

Based on this, the total large chamber sink is 1.4 – 1.9 min^{-1} and the total mini chamber sink is 1 – 3.9 min^{-1}. Since these ranges overlap considerably, it is likely that differences in new particle formation between chambers (no new particle formation in the large chamber vs. repeated new particle formation in the mini chamber) is due to large differences in total oxidation rates at the beginning of each experiment.

S.6. Nucleated particles in large chamber experiments

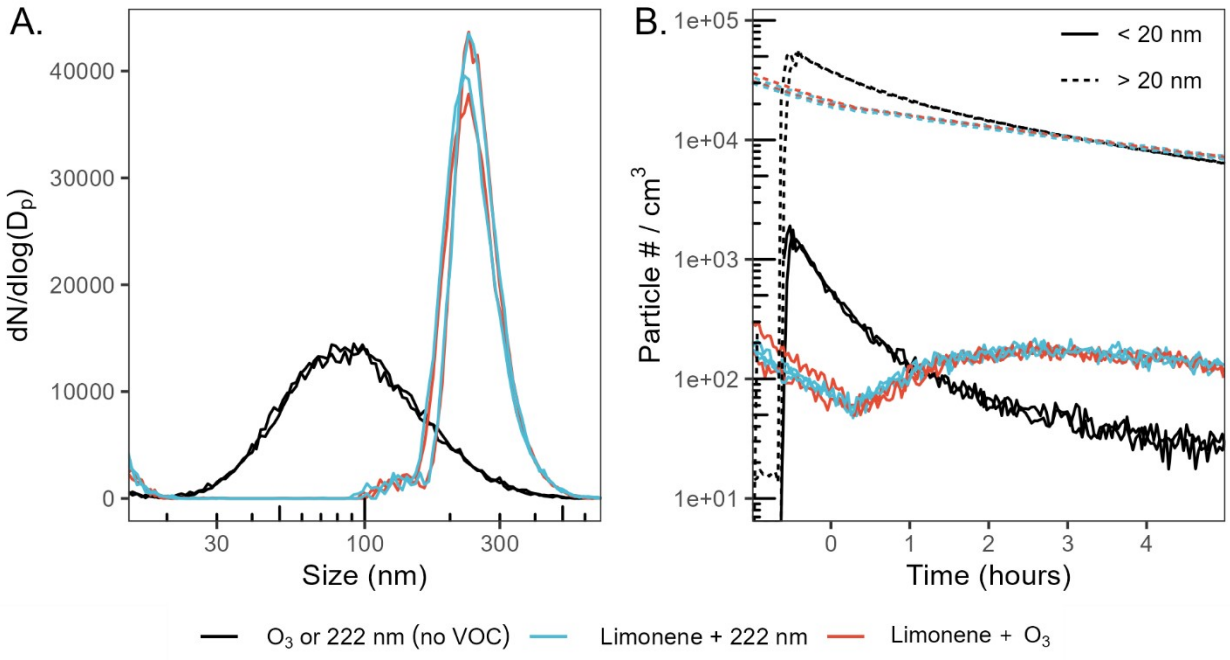

Figure S12: Example size distributions (A) and total particle concentration timeseries (B) for large chamber experiments. Panel A shows number-weighted particle size distributions at t = 4 hours for each NO_X-free large chamber experiment. Panel B shows total particle number concentration, split between particles less than and greater than 20 nm for all large chamber experiments (separated in the plot by linetype). Note the logarithmic y axis.

Figure S12 shows particle size distributions and trends in total particle number for large chamber experiments. As can be seen in Fig. S12A, experiments for which limonene was added feature a small nucleated particle mode with particles of diameter < 20 nm. This mode grows slightly in magnitude but these particles do not grow in size. In contrast, particle counts for sizes between ~20 nm and ~ 100 nm are near zero (at t = 4 hrs), since the original seed particles from this size range have grown as oxidized organics condense onto them. Note that the small < 20 nm mode does not differ between 222 nm and ozone control experiments, suggesting that this is a function of ozone chemistry. The particle size distribution for blank experiments is centered at a much smaller diameter because no particle growth has occurred through condensation of oxidized organics.

Figure S12B shows timeseries of the total particle number concentration, split between size bins less than and greater than 20 nm. After t ≈ 15 minutes, the total particle number < 20 nm in diameter increases due to the presence of the small nucleation mode. This is identical for all experiments with limonene, and does not occur in blank experiments where no VOC is added. Note that the concentration of seed aerosol is higher for blank experiments at t = 0 since we added the same amount of total seed but did not include the same waiting period to measure limonene dilution before the experiment was started; nonetheless, formation of particles < 20 nm in blank experiments is not observed even as the seed particle concentration falls throughout the experiment. No obvious growth in particle number concentration is seen for the larger size range, though the wall loss rate is slightly slower for organic coated particles.

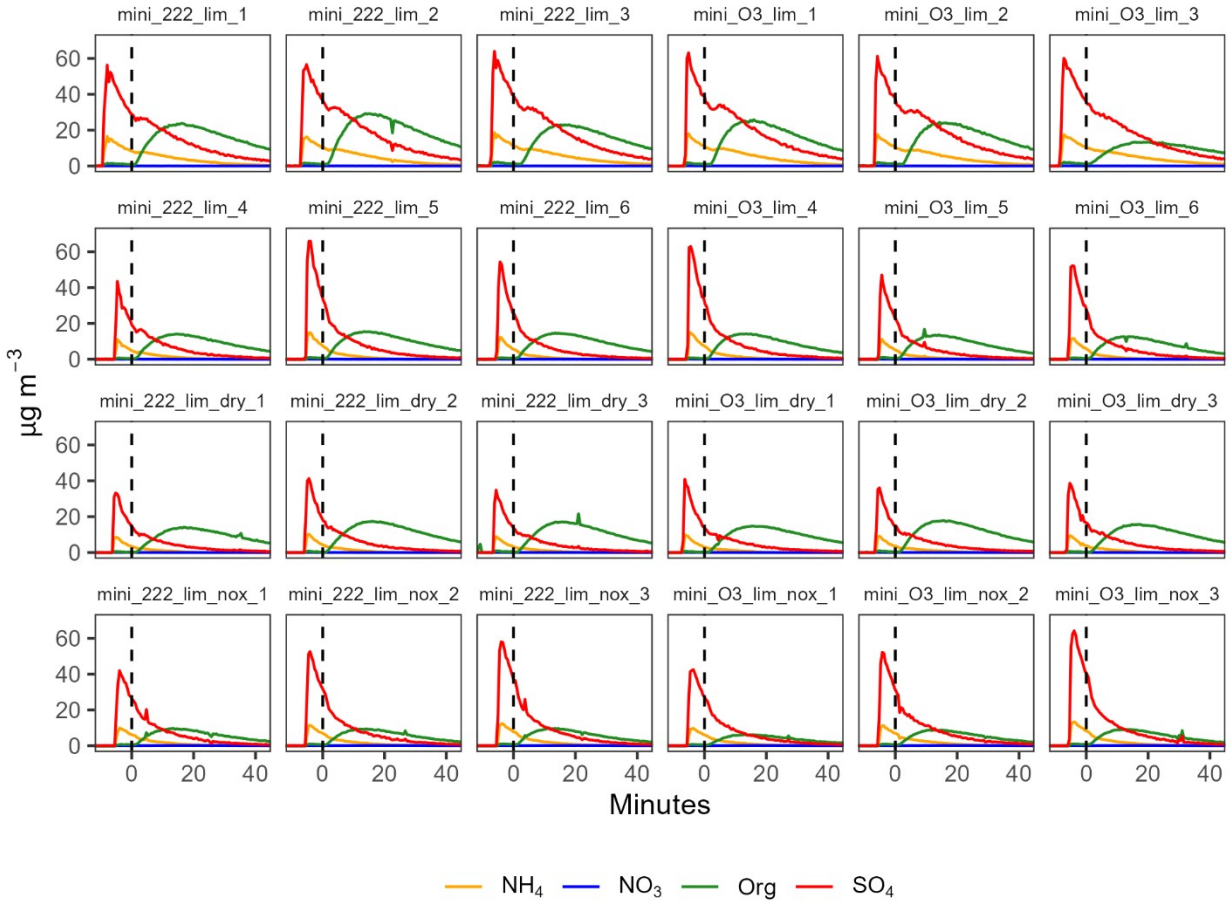

Figure S13: Aerosol composition timeseries for each mini chamber limonene experiment. Data are not corrected for wall loss, dilution loss, or collection efficiency. Each row represents a set of comparable experiments, with GUV_{222} conditions shown on the left and ozone control conditions shown on the right.

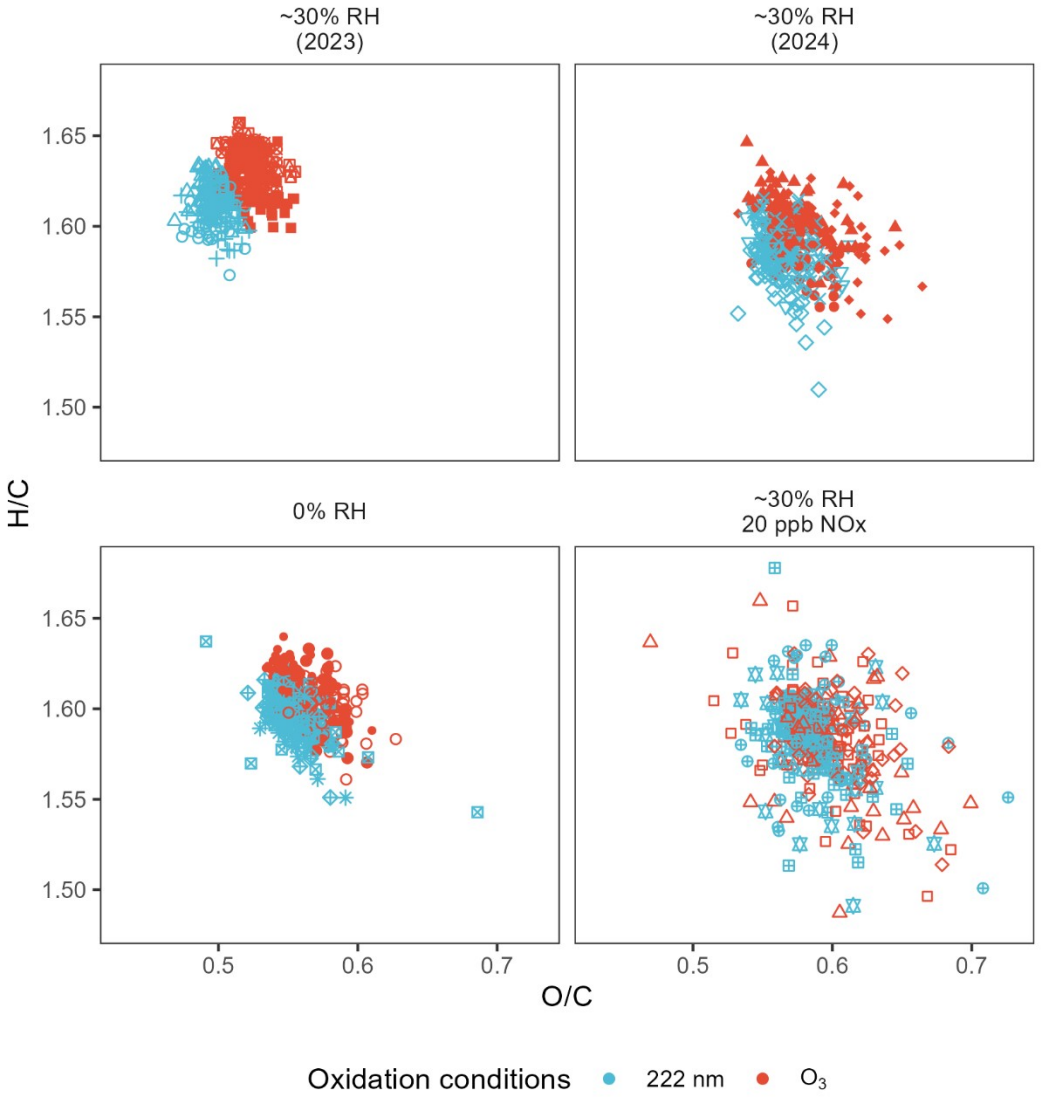

Figure S14: O/C and H/C ratios for limonene oxidation experiments in the mini chamber. Panels are separated by experiment set such that GUV_{222} and ozone-only experiments are only directly compared to experiments run under matching conditions. Each experiment is marked with a different point shape. Elemental ratios are only plotted after they have stabilized, from t = 15 to 50 min. Greater overlap between GUV_{222} and ozone control condition is seen for experiments with lower total AMS Org signal (see Fig. S13).

S.7. Modeling limonene chamber experiments using the Master Chemical Mechanism

To examine potential differences in unmeasured trace radical species between GUV_{222} and ozone control conditions, limonene experiments are modeled using the Master Chemical Mechanism (MCM)[10] implemented in the Framework for 0-D Atmospheric Modeling (F0AM).[11] This uses the MCM limonene mechanism, augmented with O_2 photolysis and O_3 photolysis reactions (rates from Table S3 of Barber et al.[1] and implemented offline). The model uses RH = 35%, T = 297 K, and dilution rate constant = 9×10^{-4} s^{-1}. The model is spun up for two hours to allow ozone to come to a steady state before 100 ppb of limonene is added. A timeseries of ozone and limonene is shown in Figure S15 to demonstrate the model setup. Calculated OH, RO_2, and HO_2 timeseries are shown in Figure S16.

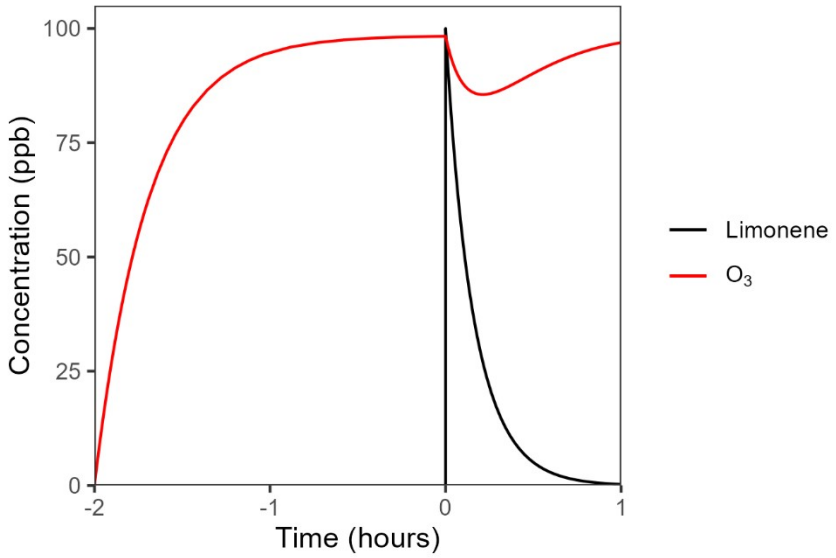

Figure S15: Modeled ozone and limonene timeseries representing a 222 nm + limonene experiment in the mini chamber. T = 0 is considered to be the time of limonene addition.

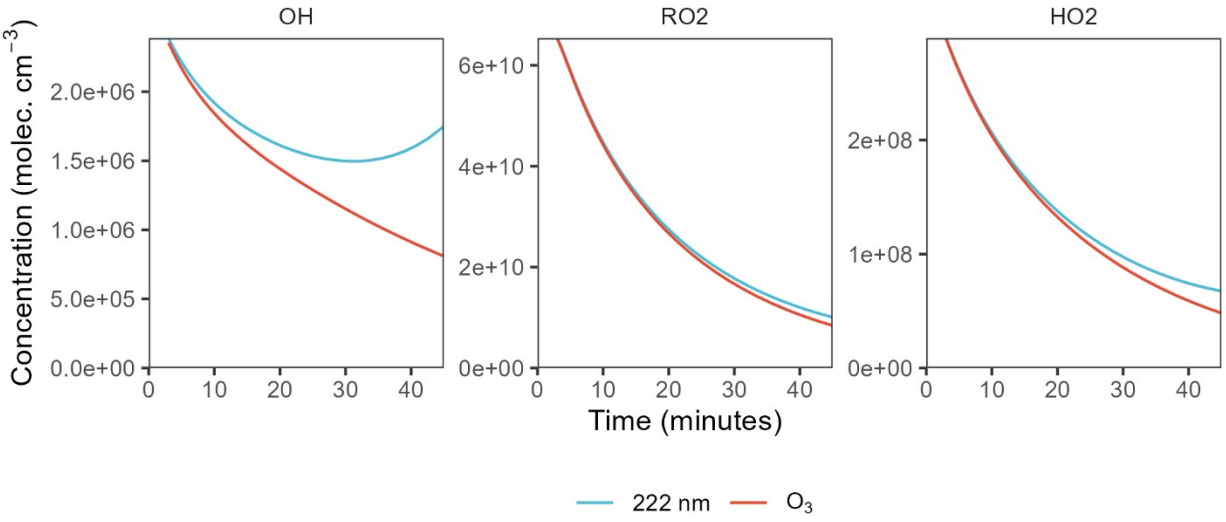

Figure S16: Modeled OH, total RO_2, and HO_2 timeseries from mini chamber limonene oxidation experiments run under GUV_{222} and ozone control conditions. Data are plotted from t = 3 min to t = 45 min. Note that the y-scale differs in each panel.

From t = 3 min to t = 45 min (avoiding instantaneous spikes in concentrations near t = 0), average OH, total RO_2, and HO_2 are 22%, 3%, and 6% greater respectively under GUV_{222} conditions than under ozone control conditions. These differences are lowest near the beginning of the experiment, when new particle formation is observed (e.g., OH is only 3% higher under GUV_{222} conditions for t = 3 – 10 min).

S.8. Photolysis of HONO and NO_2 under 222 nm light

One additional experiment was run to measure the photolysis rate of HONO under 222 nm light in the large chamber. Here, HONO was added to the chamber using the same methods as described above in Section S.2., but this time, two additions of 20 µL 1 M H_2SO_4 were used at a flow rate of 2 µL min^{-1}. Air flow through the round bottom flask was stopped when the HONO concentration reached ~33 ppb. The chamber was left undisturbed for nearly two hours before the 222 nm light was turned on. After a little over 2 hours, the 222 nm light was turned off and the normal large chamber lights (peak emission around 340 nm, $J_{NO2} \approx 1.06$ min^{-1}) were turned on. NO_X and HONO timeseries for this experiment are shown in Figure S17; these are dilution-corrected based on the total NO_X timeseries before lights were turned on, accounting for loss due to the 20 LPM clean air dilution flow.

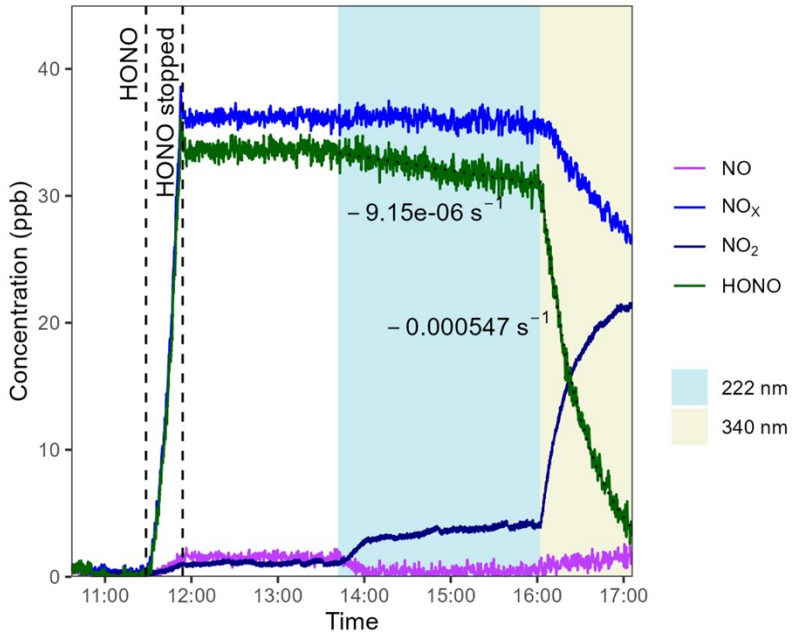

Figure S17: Dilution-corrected NO_X and HONO timeseries for an experiment measuring the photolysis rate of HONO in the large chamber under 222 nm and 340 nm light. Shaded regions show the times during which the two light sources were turned on. Exponential fits to the decay in the HONO signal are shown in dotted lines, and their exponential rate constants are annotated on the plot.

As can be seen in Figure S17, HONO is introduced to the chamber with some NO and NO_2 byproducts, but all concentrations are stable before lights are turned on, indicating that no chemistry is occurring. Once the 222 nm light is turned on, HONO decreases gradually, with a measured $J_{HONO,222\ nm} = 9.15 \times 10^{-6}$ s^{-1}. All NO is converted to NO_2 to reaction with O_3 produced by the 222 nm light. When the 340 nm lights are turned on, the photolysis rate of HONO increases dramatically (measured $J_{HONO,\ 340\ nm} = 5.47 \times 10^{-4}$ s^{-1}), NO_2 formation is accelerated, steady-state NO increases slightly, and total measured NO_X signal is observed to decrease, likely due to the formation of HNO_3 which is not detected.

Photolysis rates for HONO and NO_2 can also be calculated based on literature cross sections. For NO_2, the photolysis rate cannot be measured easily under 222 nm light because high ozone concentrations keep [NO] below the detection limit of the NO_X monitor (NO concentration is necessary for using the standard steady-state relationship $J_{NO2} = k_{O3+NO}[NO][O_3] / [NO_2]$). Using reference cross section data (HONO cross section from JPL[12] and NO_2 cross section from IUPAC[13]) and the same 222 nm light spectrum as used in Barber et al.,[1] the HONO and NO_2 photolysis rates under 222 nm light are calculated to be 5.3×10^{-6} s^{-1} and 1.8×10^{-6} s^{-1} (large chamber, GUV_{222} fluence rate ≈ 3.9 µW cm^{-2}), and 6.1×10^{-5} s^{-1} and 2.0×10^{-5} s^{-1} (small chamber, GUV_{222} fluence rate = 45 µW cm^{-2}) respectfully. For HONO, the measured value is slightly above the calculated value but is still in reasonable agreement. These photolysis rates are well below the rates of photolysis under the 340 nm lights of the large chamber (4.1×10^{-4} s^{-1} for HONO, 1.8×10^{-3} s^{-1} for NO_2) and for typical outdoor conditions ($J_{HONO,outdoor} \approx 5 \times 10^{-4}$ s^{-1}, $J_{NO2,outdoor} \approx 3 \times 10^{-3}$ s^{-1} using the ASTM G173-03 reference spectrum). Furthermore, the 222 nm photolysis rates at these fluence rates are slower than dilution loss. For comparison, 1 air change per hour (ACH), a typical indoor air exchange rate, corresponds to a 2.8×10^{-4} s^{-1} loss rate, indicating that

NO_2 and HONO should be lost much faster to dilution than to photolysis under any reasonable GUV_{222} light fluence rate.

S.9. Oxidized gas-phase organics measurements

As discussed previously, the NH_4^+ CIMS was used for some experiments and while the instrument was not fully functional, it can be used to make qualitative observations of oxidized gas-phase organic molecules. Figure S18 shows unit mass resolution timeseries of three of the most abundant observed ions, as well as two of the most abundant ions over m/z 300 for the series of humid limonene mini chamber experiments carried out in 2024 (panels a – e) and for the limonene mini chamber experiments with steady-state added NO_X (panels f – j). Note that data for two NO_X-free and one NO_X experiment are plotted with dotted lines to indicate that the instrument output was unstable at that time, with a different distribution of primary ions and a dramatically different product mass spectrum. While these plots represent only a selection of ions detected by the mass spectrometer, no systematic differences between GUV_{222} and O_3 only conditions are observed, with all timeseries following remarkably similar profiles.

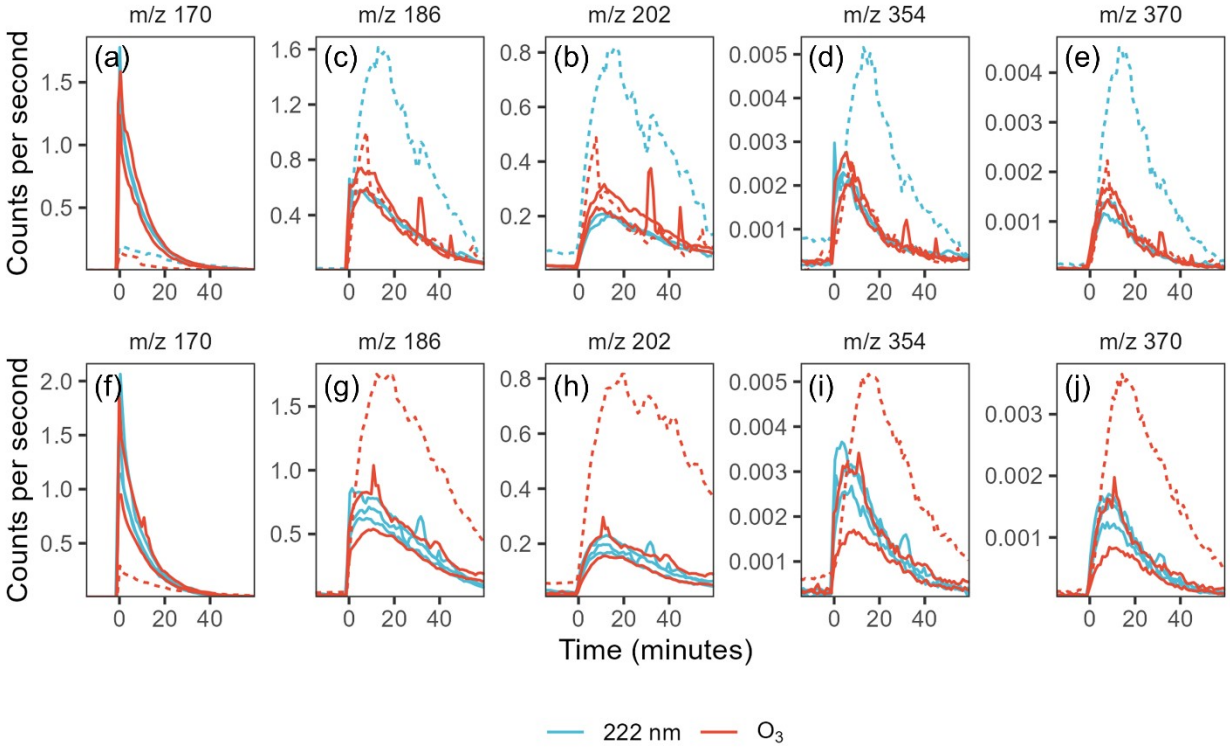

Figure S18: Selected NH_4^+ CIMS unit mass resolution ion timeseries from NO_X-free humid mini chamber experiments (expts. 21 – 26) (Panels a – e) and from experiments with steady-state NO_X (expts. 27 – 32) (Panels f – j). Each panel shows timeseries from a single unit mass resolution ion signal for all six of the grouped experiments. Color refers to oxidant condition. The values shown here are in raw counts per seconds. Three experiments (expts. 22, 23, 32) are plotted with dotted lines to indicate that the instrument was unstable (atypical primary ion distribution with a low total signal) when taking these data. The left three columns (Panels a – c, f – h) show three of the most abundant observed ions, while the right two columns (Panels d, e, i, j) show two of the most abundant ions over m/z 300.

S.10. References

1 V. P. Barber, M. B. Goss, L. J. Franco Deloya, L. N. LeMar, Y. Li, E. Helstrom, M. Canagaratna, F. N. Keutsch and J. H. Kroll, Indoor Air Quality Implications of Germicidal 222 nm Light, *Environ. Sci. Technol.*, 2023, **57**, 15990–15998.

2 M. R. Canagaratna, J. L. Jimenez, J. H. Kroll, Q. Chen, S. H. Kessler, P. Massoli, L. Hildebrandt Ruiz, E. Fortner, L. R. Williams, K. R. Wilson, J. D. Surratt, N. M. Donahue, J. T. Jayne and D. R. Worsnop, Elemental ratio measurements of organic compounds using aerosol mass spectrometry: characterization, improved calibration, and implications, *Atmospheric Chem. Phys.*, 2015, **15**, 253–272.

3 N. Wang, S. D. Jorga, J. R. Pierce, N. M. Donahue and S. N. Pandis, Particle wall-loss correction methods in smog chamber experiments, *Atmospheric Meas. Tech.*, 2018, **11**, 6577–6588.

4 M. B. Goss and J. H. Kroll, Chamber studies of OH + dimethyl sulfoxide and dimethyl disulfide: insights into the dimethyl sulfide oxidation mechanism, *Atmospheric Chem. Phys.*, 2024, **24**, 1299–1314.

5 K. H. Liland and B.-H. Mevik, baseline: Baseline Correction of Spectra, version 1.3-5, 2023.

6 A. Zaytsev, M. Breitenlechner, A. R. Koss, C. Y. Lim, J. C. Rowe, J. H. Kroll and F. N. Keutsch, Using collision-induced dissociation to constrain sensitivity of ammonia chemical ionization mass spectrometry (NH_4^+ CIMS) to oxygenated volatile organic compounds, *Atmospheric Meas. Tech.*, 2019, **12**, 1861–1870.

7 T. Benaglia, D. Chauveau, D. R. Hunter and D. Young, mixtools : An *R* Package for Analyzing Finite Mixture Models, *J. Stat. Softw.*, 2009, **32**, 1–29.

8 J. E. Krechmer, D. A. Day and J. L. Jimenez, Always Lost but Never Forgotten: Gas-Phase Wall Losses Are Important in All Teflon Environmental Chambers, *Environ. Sci. Technol.*, 2020, **54**, 12890–12897.

9 Q. Ye, M. B. Goss, G. Isaacman-VanWertz, A. Zaytsev, P. Massoli, C. Lim, P. Croteau, M. Canagaratna, D. A. Knopf, F. N. Keutsch, C. L. Heald and J. H. Kroll, Organic Sulfur Products and Peroxy Radical Isomerization in the OH Oxidation of Dimethyl Sulfide, *ACS Earth Space Chem.*, 2021, **5**, 2013–2020.

10 S. M. Saunders, M. E. Jenkin, R. G. Derwent and M. J. Pilling, Protocol for the development of the Master Chemical Mechanism, MCM v3 (Part A): tropospheric degradation of non-aromatic volatile organic compounds, *Atmospheric Chem. Phys.*, 2003, **3**, 161–180.

11 G. M. Wolfe, M. R. Marvin, S. J. Roberts, K. R. Travis and J. Liao, The Framework for 0-D Atmospheric Modeling (F0AM) v3.1, *Geosci. Model Dev.*, 2016, **9**, 3309–3319.

12 J. Burkholder, S. P. Sander, J. P. D. Abbatt, J. R. Barker, C. Cappa, J. D. Crounse, T. S. Dibble, R. E. Huie, C. E. Kolb, M. J. Kurylo, V. L. Orkin, C. J. Percival, D. M. Wilmouth and P. H. Wine, *Chemical Kinetics and Photochemical Data for Use in Atmospheric Studies*, NASA Jet Propulsion Laboratory, 2020.

13 R. Atkinson, D. L. Baulch, R. A. Cox, J. N. Crowley, R. F. Hampson, R. G. Hynes, M. E. Jenkin, M. J. Rossi and J. Troe, Evaluated kinetic and photochemical data for atmospheric chemistry: Volume I - gas phase reactions of O_X, HO_X, NO_X and SO_X species, *Atmospheric Chem. Phys.*, 2004, **4**, 1461–1738.